

Transition from Homogeneous to Domain-Wall-Mediated Polarization Switching in BaTiO₃: A Machine-Learning Molecular Dynamics Study

Po-Yen Chen,^{1,*} Teruyasu Mizoguchi,^{1,2,†}

¹Department of Materials Engineering, the University of Tokyo, 153-8505 Tokyo, Japan.

²Institute of Industrial Science, the University of Tokyo, 113-0033 Tokyo, Japan.

ABSTRACT. Polarization switching in ferroelectric BaTiO₃ can proceed through fundamentally different mechanisms — yet the conditions that determine which pathway is realized remain poorly understood. Using machine-learning potential-based molecular dynamics with the MACEField model, we systematically vary supercell size to reveal a clear transition from homogeneous polarization switching to domain-wall-mediated switching, accompanied by a coercive field increase of over 50%. Shannon entropy analysis demonstrates that this transition is driven by size-dependent polarization fluctuations that promote 180° domain-wall nucleation — establishing a direct, quantitative link between local configurational disorder and macroscopic switching behavior. Furthermore, the switching pathway and hysteresis response are shown to depend critically on supercell geometry and the relative orientation of applied stress and electric field. These findings reveal that homogeneous and domain-wall-mediated switching are distinct physical regimes in BaTiO₃, and that atomistic simulations must account for system size to correctly capture the operative switching mechanism.

I. INTRODUCTION.

Ferroelectric polarization behavior plays a crucial role in determining the functional properties of ferroelectric materials, including dielectric response, piezoelectricity, and non-volatile switching characteristics[1-5]. Among various ferroelectric materials, tetragonal BaTiO₃ has been extensively studied as a prototypical perovskite ferroelectric owing to its well-known spontaneous polarization, multiple structural phase transitions, and strong electromechanical coupling[6-10]. In tetragonal BaTiO₃, ferroelectricity originates from the off-center displacement of Ti ions within the oxygen octahedra, leading to spontaneous polarization along the crystallographic *c*-axis. The polarization state is strongly coupled to lattice distortion and domain configuration, making polarization switching highly sensitive to external electric fields and mechanical constraints[11-14].

Despite extensive experimental [15-20] and computational investigations[11,21-23], a fundamental question remains open: polarization switching in BaTiO₃ can proceed through qualitatively different pathways, homogeneous reversal or domain-wall-mediated switching, yet the conditions that determine which mechanism is operative are poorly understood. In homogeneous switching, polarizations collectively reverse throughout the crystal, accompanied by coherent lattice deformation, frequently through a two-step pathway involving transient polarization rotation and intermediate polarization states[11,21]. In contrast, domain-wall-mediated switching proceeds through local domain nucleation and subsequent domain-wall (DW)

propagation[12,22-24]. These two mechanisms represent fundamentally different microscopic and macroscopic polarization dynamics and therefore lead to distinct coercive fields, switching kinetics, and electromechanical responses. Therefore, clarifying the competition between homogeneous and DW-mediated switching is essential for understanding the intrinsic ferroelectric behavior of BaTiO₃ and for improving the performance of ferroelectric-based devices.

Previous atomistic simulations have reported apparently different switching behaviors depending on the simulation conditions: NVT-based simulations[22] tend to favor domain nucleation and domain-wall formation, whereas NPT-based simulations[11,21] more frequently exhibit homogeneous polarization switching. However, it remains unclear whether these differences primarily originate from the choice of simulation ensemble or reflect an intrinsic physical crossover in ferroelectric switching behavior. Clarifying this distinction is essential not only for interpreting atomistic simulations, but also for understanding the microscopic origin of coercive fields and switching kinetics in real ferroelectric systems.

The stability of homogeneous and DW-mediated switching is expected to strongly depend on the accessible length scale, strain accommodation, and geometric constraints of the system. In our previous study,[11] based on NPT simulations with fully relaxable lattice degrees of freedom, we observed that larger BaTiO₃ supercells under compressive stress conditions tend to stabilize 180° DW structures during polarization switching, suggesting a crossover from homogeneous collective switching to domain-

*Contact author: poyen@iis.u-tokyo.ac.jp

†Contact author: teru@iis.u-tokyo.ac.jp

mediated polarization reversal as the system size increases. Nevertheless, the relationship between supercell size, domain stability, and switching mechanism has not yet been systematically clarified.

Therefore, in the present study, we systematically investigate the influence of supercell size and geometry on polarization switching behavior in tetragonal BaTiO₃ using machine learning potential-based molecular dynamics (MLP-MD) simulations under external electric fields within the NPT ensemble. By varying the accessible length scale under strain-relaxing conditions, we analyze hysteresis loops and polarization switching processes. Particular attention is given to the emergence of DW-mediated switching, its onset conditions, and its influence on ferroelectric properties, including coercive fields, switching pathways, and electromechanical responses in BaTiO₃.

II. METHODS

A. MLP and BEC model

In this study, we employed the MLP-MD framework developed in our previous works[11,25]. The interatomic interactions were described using our previously finetuned MACE model[26], while the Born effective charge (BEC) was predicted using the MACEfield-finetuned model[27]. Compared with the previously developed Equivar model[28,29], the MACEfield model provides significantly faster BEC calculations for large supercell systems. The computational performance of the MACEfield model is summarized in Section SI.3 of the Supplementary Information. The finetuned MACE model was developed based on the pretrained MACE-MP-0 foundation model[30,31] and further finetuned using our BaTiO₃ dataset containing 4,045 2×2×2 BaTiO₃ structures with the PBEsol functional[26]. Since the present study focuses on solid-state BaTiO₃ systems, a subset containing 2,038 solid-phase structures with BEC data[11] calculated by density functional perturbation theory (DFPT)[32,33] implemented in Vienna Ab initio Simulation Package (VASP)[34-36] was selected from the database for the MACEfield training. The MACEfield model was then further finetuned based on the previously trained MACE model. The final MACEfield model achieved a mean absolute error (MAE) of approximately 0.01 for the BEC prediction of solid-state structures, which is significantly smaller than the corresponding MAE of 0.03 obtained using the previous Equivar model.

B. MLP-MD workflow and hysteresis-loop simulations

After constructing the MLP and BEC models, we employed the MLP-MD framework to investigate the electric-field response of ferroelectric tetragonal

BaTiO₃ systems. During each MD step, the total force acting on atoms was calculated as $F_{total} = F_{MLP} + Z \cdot \varepsilon$, where F_{MLP} is the interatomic force predicted by the MLP, Z is the BEC, and ε is the external electric field. This framework was implemented within the atomic simulation environment (ASE)[37] package under the NPT ensemble to enable MD simulations under finite electric fields. To further accelerate the MD simulations and improve computational efficiency for large supercell systems, cuEquivariance acceleration[38] was employed during the MACE/MACEfield calculations. The computational performance improvement obtained using cuEquivariance is discussed in Appendix A.

For the P-E hysteresis-loop simulations, we employed the Nosé-Hoover thermostat together with the Parrinello-Rahman barostat within the NPT ensemble[39,40]. In the present study, the maximum electric-field amplitude was increased to 150 kV/cm, compared with 100 kV/cm in our previous work[11]. To maintain a comparable electric-field sweeping rate and minimize rate-dependent effects on the hysteresis behavior, the total MD simulation steps were increased from 400,000 to 600,000 steps. Consequently, the electric-field scanning frequency was adjusted from 2.5 GHz to 1.67 GHz.

C. Ti-displacement calculations

In order to analyze the local polarization behavior in BaTiO₃, we evaluated the displacement of Ti atoms relative to the centers of their surrounding oxygen coordination environments. In tetragonal BaTiO₃, spontaneous polarization originates primarily from the off-center displacement of Ti atoms within TiO₆ octahedra. Therefore, the local polarization direction can be characterized using the Ti off-center displacement vector. For each Ti atom, neighboring oxygen atoms within a cutoff radius of 3 Å were identified using a neighbor-search algorithm. The geometric center of the surrounding oxygen atoms was calculated as $\mathbf{R}_{env,O} = \frac{1}{N} \sum_{i=1}^N \mathbf{R}_{i,O}$, where N is the number of neighboring oxygen atoms and $\mathbf{R}_{i,O}$ denotes the Cartesian coordinates of each neighboring oxygen atom. The local Ti-displacement vector was then defined as $\Delta\mathbf{R}_{Ti} = \mathbf{R}_{Ti} - \mathbf{R}_{env,O}$, where \mathbf{R}_{Ti} is the Ti atomic position. This displacement vector was used to characterize the local polarization direction and analyze polarization distributions and domain structures in BaTiO₃.

III. RESULTS and DISCUSSION

A. Size-dependent P-E hysteresis loop and micro polarization behavior along the b-axis electric field

*Contact author: poyen@iis.u-tokyo.ac.jp

†Contact author: teru@iis.u-tokyo.ac.jp

First, we investigated the evolution of polarization switching behavior with increasing supercell size along the c axis. Since the stress-induced DW structures preferentially formed along the a/b -axis orientation in our previous observations[11], and considering the symmetry of the tetragonal structure, triangular electric fields were first applied along the b axis. The maximum electric field amplitude and frequency were set to 150 kV/cm and 1.67 GHz, respectively. To examine the finite-size effect, the supercell size was systematically increased from $8 \times 8 \times 8$ to $8 \times 8 \times 32$. The resulting P-E hysteresis loops are presented in Figure 1. Although the remanent polarization remains nearly unchanged with increasing supercell size, a significant increase in the averaged coercive field is observed for supercells larger than $8 \times 8 \times 16$. Specifically, the coercive field increases from approximately 55 kV/cm for the $8 \times 8 \times 8$ supercell to approximately 85 kV/cm for the larger supercells. Moreover, the coercive field becomes nearly size-independent beyond the $8 \times 8 \times 16$ supercell. This distinct change in coercive behavior suggests that the underlying polarization switching mechanism in larger supercells differs from that in the smaller $8 \times 8 \times 8$ system.

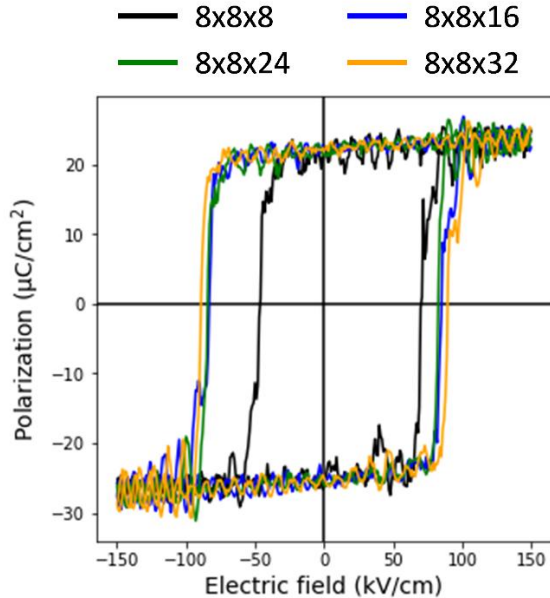


Figure 1 Size-dependent hysteresis loops of the $8 \times 8 \times n$ tetragonal BaTiO_3 supercell at 250 K under zero mechanical stress. The black, blue, green, and orange lines represent the P-E curve with $n = 8, 16, 24,$ and 32 , respectively.

To further investigate the polarization-switching mechanism, we analyzed the local polarization based on Ti displacements. Figure 2 presents the local polarization projected onto the bc plane in the $8 \times 8 \times 32$

supercell during polarization switching, where the arrows indicate the local polarization directions. As shown in the figure, local polarization reversal first emerges inside the supercell (step 97), indicating the nucleation of an oppositely polarized domain. With continued electric-field application, the nucleated domain gradually expands (steps 98 and 99) and eventually produces complete polarization reversal (step 150) through the formation and propagation of a 180° DW. As discussed in previous Monte Carlo studies[41,42] and our earlier investigation of stress-induced 180° DW[11], the formation of a 180° DW is associated with a positive formation energy. This suggests that the domain-nucleation switching pathway requires overcoming an additional energy barrier compared with homogeneous switching. Such behavior is consistent with the increase in coercive field observed for larger supercells in Figure 1.

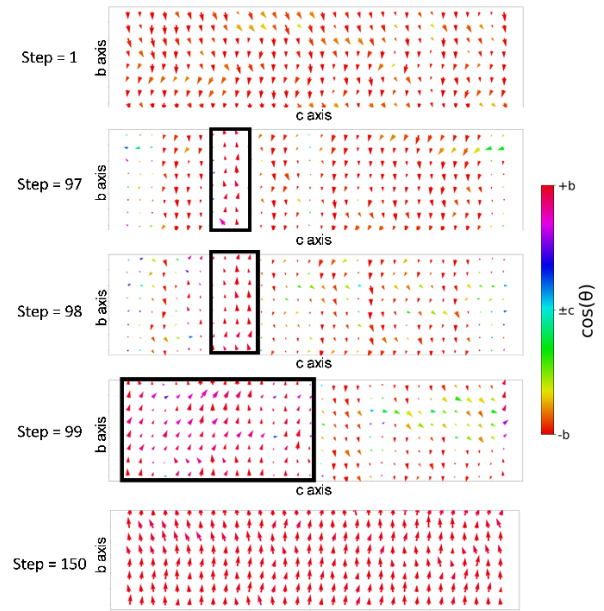


Figure 2 Evolution of Ti displacement vectors in the $8 \times 8 \times 32$ supercell at selected MD steps under a triangular electric field (maximum field: 150 kV/cm) along the b axis at 250 K. The arrows show the Ti-displacements on each Ti atom, and the circled region shows the opposite domain nuclei.

As discussed in our previous study on stress-induced DW formation[11], larger supercells exhibit a higher probability of forming DW structures during polarization switching. To further quantify this behavior, we employed Shannon entropy analysis[43] to characterize the degree of polarization fluctuation within the supercell. The calculation for Shannon entropy is mentioned in Appendix B. As shown in Figure 3, the Shannon entropy increases with supercell size, indicating enhanced polarization fluctuations in

larger systems. Such increased fluctuations may facilitate the local instability required for DW nucleation. Consequently, larger supercells tend to favor DW-mediated switching pathways, leading to polarization reversal through domain nucleation and growth. In contrast, smaller supercells exhibit reduced polarization fluctuations, which suppress local nucleation events and instead favor homogeneous polarization switching. This behavior is also consistent with the higher coercive field observed in larger supercells.

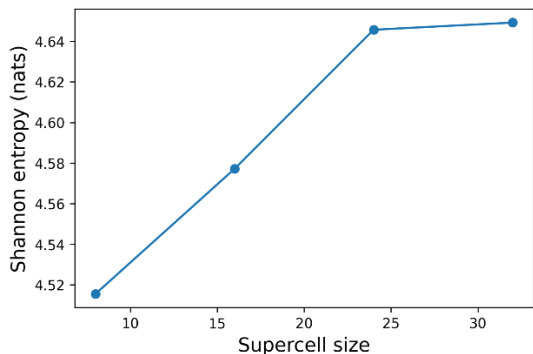


Figure 3 Size-dependent Shannon Entropy of the $8 \times 8 \times n$ tetragonal BaTiO_3 supercell at 250 K.

Furthermore, the domain-nucleation process observed here is qualitatively similar to that reported by Falletta et al.[22] However, their simulations were performed under the NVT ensemble, in which the simulation cell shape is constrained and cannot deform during switching. Recent NPT-based MD simulations[11,21], LGD calculations[24], and experimental studies[17-19] have suggested that polarization switching preferentially proceeds via a two-step pathway ($c \rightarrow a/b \rightarrow -c$), since this pathway generally exhibits a lower activation barrier[24]. Because this mechanism is accompanied by lattice deformation, the constrained cell shape in NVT simulations suppresses polarization rotation and favors direct polarization reversal[22]. As a result, domain nucleation becomes more favorable, leading to a larger coercive field compared with our previous study[11]. This may explain why Falletta et al.[22] observed domain nucleation even in relatively small supercells, whereas homogeneous switching was not reported. In contrast, the two-step polarization-switching pathway observed in our simulations is accompanied by clear lattice deformation, as shown for the $8 \times 8 \times 32$ supercell in Figure 4. Therefore, although both our work and the study by Falletta et al.[22] exhibit domain nucleation during polarization switching, the underlying switching mechanisms are substantially different.

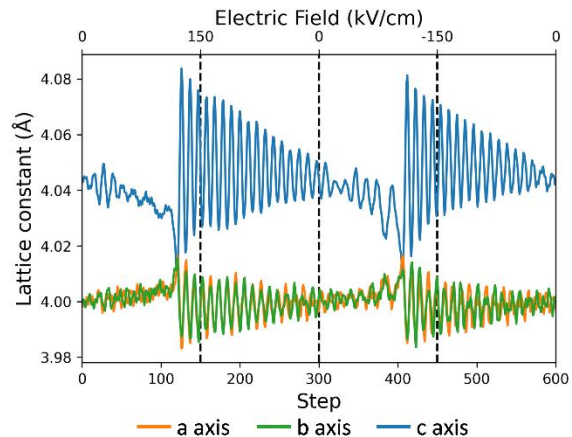


Figure 4 The step-dependent lattice constant of an $8 \times 8 \times 32$ tetragonal supercell under the triangular electric field. The orange, green, and blue lines represent the a, b, and c axes, respectively.

B. Electric field orientation-dependent P-E hysteresis behavior

To investigate the anisotropic influence of electric-field orientation on polarization switching, we analyzed the P-E hysteresis behavior of the $8 \times 8 \times 32$ supercell under a c-axis electric field and compared it with the b-axis electric-field case and the smaller $8 \times 8 \times 8$ supercell as shown in Figure 5. As shown in the figure, the $8 \times 8 \times 32$ supercell under the c-axis electric field exhibits a substantially larger coercive field, reaching approximately 110 kV/cm, compared with both the smaller supercell and the b-axis electric-field case (~ 85 kV/cm). This increase suggests that polarization reversal under the c-axis electric field is associated with a larger effective switching barrier and is no longer dominated by homogeneous switching. Furthermore, the noticeable difference between the b-axis and c-axis electric-field cases indicates that the polarization-switching behavior in the elongated $8 \times 8 \times 32$ supercell is strongly anisotropic and depends sensitively on the electric-field orientation relative to the supercell geometry.

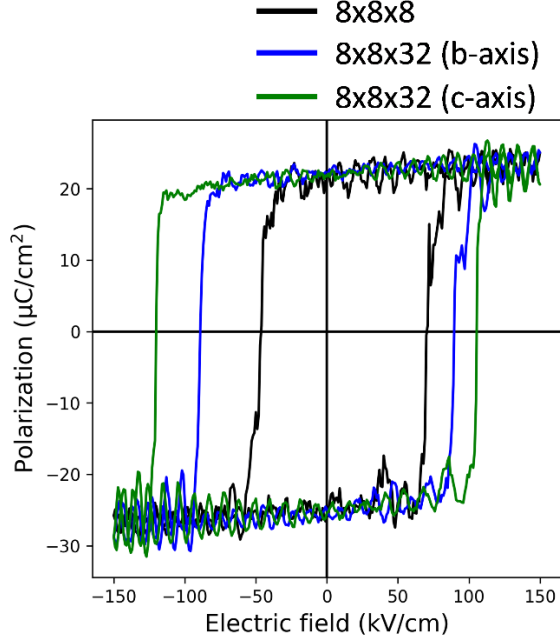


Figure 5 Electric field orientation-dependent hysteresis loops of the $8 \times 8 \times 8$ and $8 \times 8 \times 32$ tetragonal BaTiO_3 supercell at 250 K. The black, blue, green, and orange lines represent the hysteresis loop of the $8 \times 8 \times 8$ supercell, the $8 \times 8 \times 32$ supercell with the b-axis electric field, and the $8 \times 8 \times 32$ supercell with the c-axis electric field.

To compare the differences in switching behavior between the b-axis and c-axis electric fields, we further analyzed the evolution of local Ti displacements projected onto the bc plane during polarization reversal in the $8 \times 8 \times 32$ supercell under the c-axis electric field, as shown in Figure 6. Initially, without an external electric field (step 1), the local Ti displacements are predominantly aligned along the +c direction, accompanied by slight fluctuations toward the b direction. The polarization reversal process under the c-axis electric field is characterized by enhanced lateral polarization fluctuations and transient formation of intermediate DW-like configurations near the coercive field (step 118). As the opposite electric field approaches the coercive field, fluctuations along the b axis become significantly enhanced, accompanied by the emergence of local polarization regions oriented close to the $\langle 011 \rangle$ and $\langle 0\bar{1}\bar{1} \rangle$ directions. These intermediate polarization features resemble transient 90° DW-like structures and indicate the development of local polarization inhomogeneity during switching. Near the coercive field, the local polarizations collectively rotate toward the $\pm b$ directions together with the formation of a clear 180° DW (step 119), followed by rapid reorientation toward the $-c$ direction after switching (step 120).

These observations demonstrate that polarization reversal under the c-axis electric field proceeds through a DW-mediated switching pathway rather than homogeneous collective switching.

Notably, although both the b-axis and c-axis electric fields exhibit 180° DW formation during switching, their microscopic switching behaviors are substantially different. Under the c-axis electric field, the polarization rotation occurs more collectively near the coercive field, whereas under the b-axis electric field, the domain growth process is gradual. We suggest that this difference may originate from finite-size effects associated with the simulation cell geometry. Because the a and b directions contain only eight unit cells, the periodic boundary conditions impose stronger lateral constraints on the formation and propagation of DWs along these directions. As a result, the system tends to preserve the c-axis polarization character while forming intermediate 90° DW-like configurations during switching. In contrast, the elongated c-axis direction in the $8 \times 8 \times 32$ supercell allows greater spatial polarization variation and facilitates DW-mediated switching. However, because the polarization rotation under the c-axis electric field occurs more collectively rather than through gradual domain growth, the switching process may require overcoming a larger effective energy barrier. This behavior is consistent with the larger coercive field observed under the c-axis electric field compared with the b-axis electric field.

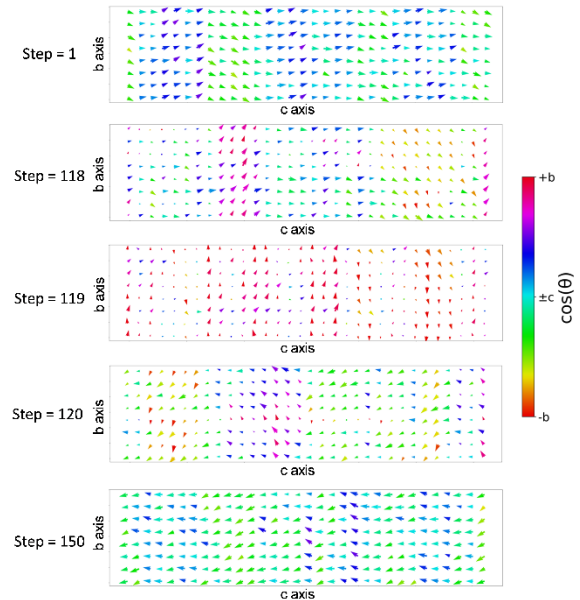


Figure 6 Evolution of Ti displacement vectors in the $8 \times 8 \times 32$ supercell at selected MD steps under a triangular electric field (maximum field: 150 kV/cm) along the c-axis at 250 K. The arrows show the Ti-displacements on each Ti atom.

C. Stress-dependent P-E hysteresis loop

To further investigate the electromechanical effects in large supercells, we applied uniaxial compressive stress to the $8 \times 8 \times 32$ supercell and analyzed its influence on the polarization-switching behavior under electric fields applied along the b and c axes. We first considered the case in which both the uniaxial compressive stress and the triangular electric field were applied along the b axis. Based on our previous studies[11], the critical compressive stress required to induce polarization rotation from the c -axis to the a/b -axis is approximately 120 MPa. To investigate the influence of uniaxial compressive stress below and above this critical value, stresses of 80 and 160 MPa were employed in this study. The resulting P-E hysteresis loops are presented in Figure 7. As shown in the figure, double hysteresis loops are observed under uniaxial compressive stresses of 80 and 160 MPa, consistent with our previous stress-related investigations[11]. As discussed in our earlier study, compressive stress parallel to the switching direction energetically favors polarization states perpendicular to the electric field, thereby stabilizing intermediate polarization configurations during the switching process and producing characteristic double hysteresis behavior.

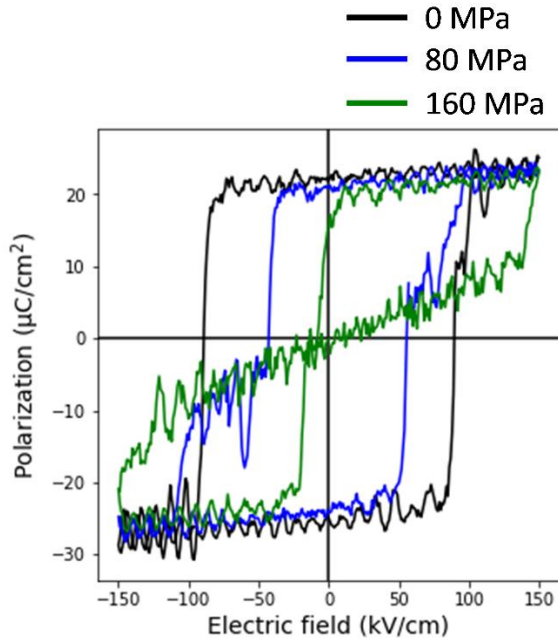


Figure 7 The P-E hysteresis loops under the b -axis electric field for the $8 \times 8 \times 32$ tetragonal BaTiO_3 supercell at 250 K under different b -axis compressive stresses. The black, blue, and green curves correspond to compressive stresses of 0, 80, and 160 MPa, respectively.

Compared with the smaller supercell case examined in our earlier study[11], the $8 \times 8 \times 32$ supercell exhibits a noticeably larger coercive field during the first polarization-switching process, suggesting the presence of a larger effective switching barrier associated with the large-supercell switching mechanism. Furthermore, unlike the smaller-supercell case, where a paraelectric-like P-E response emerged under high compressive stress, the large supercell still maintains a double hysteresis loop even at 160 MPa. This difference may originate from the larger electric-field amplitude employed in the present study, which enables polarization reversal to occur despite the mechanically stabilized intermediate polarization states. In addition, the electric-field region corresponding to the intermediate polarization state becomes noticeably wider under 160 MPa than under 80 MPa, indicating that stronger compressive stress further stabilizes the metastable polarization configuration and enlarges the metastable switching region. This behavior suggests that the competition between electric-field-driven polarization reversal and stress-induced stabilization of perpendicular polarization states becomes increasingly pronounced under stronger compressive stress. As a result, the system remains trapped within intermediate polarization configurations over a broader electric-field range before complete polarization reversal occurs.

To further clarify the orientation dependence of this electromechanical coupling, we next considered the case in which the compressive stress was applied perpendicular to the polarization-switching direction. In this configuration, uniaxial compressive stress was applied along the c axis, whereas the triangular electric field was applied along the b axis in the $8 \times 8 \times 32$ supercell. In contrast to the parallel-field case, the hysteresis loops remain nearly unchanged even under compressive stress up to 160 MPa. Neither double hysteresis behavior nor a significant change in coercive field is observed, indicating that compressive stress applied perpendicular to the switching direction has only a limited influence on the polarization-switching dynamics. These results demonstrate that the influence of uniaxial compressive stress on polarization switching strongly depends on its relative orientation with respect to the electric-field direction. When the compressive stress is applied parallel to the switching direction, intermediate polarization states become energetically stabilized, substantially modifying the switching pathway and hysteresis behavior. In contrast, compressive stress applied perpendicular to the switching direction couples only weakly to the polarization reversal process and therefore produces minimal changes in the ferroelectric response.

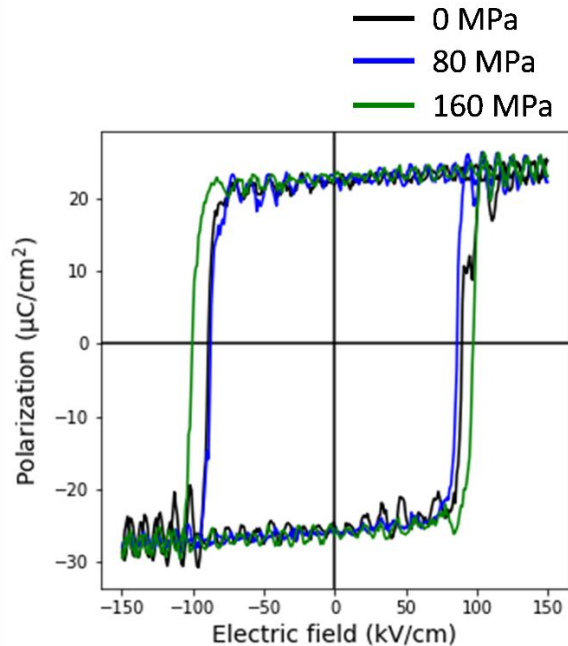


Figure 8 The P–E hysteresis loops under the *b*-axis electric field for the $8\times 8\times 32$ tetragonal BaTiO_3 supercell at 250 K under different *c*-axis compressive stresses. The black, blue, and green curves correspond to compressive stresses of 0, 80, and 160 MPa, respectively.

Based on the above observations, the influence of uniaxial compressive stress on the hysteresis behavior is strongly dependent on its orientation relative to the electric-field direction. In the case where both the uniaxial compressive stress and the triangular electric field are applied along the *c* axis of the $8\times 8\times 32$ supercell, the emergence of double hysteresis behavior becomes significantly suppressed compared with the *b*-axis electric-field case, as shown in Figure 9. This behavior suggests that increasing the supercell dimension along the stress and electric-field direction weakens the effective constraints imposed by periodic boundary conditions, thereby enhancing local polarization fluctuations and configurational freedom within the system. As a result, the stress-induced stabilization of polarization states perpendicular to the electric-field direction becomes partially relaxed, making the formation of intermediate polarization states more difficult.

Consistent with this interpretation, the system retains a single hysteresis loop under compressive stresses of 80 and 120 MPa, despite a substantial reduction in the coercive field. Double hysteresis behavior emerges only when the compressive stress reaches 160 MPa, whereas smaller supercells and the *b*-axis electric-field case exhibit double hysteresis loops already at 80 MPa. These results indicate that the

critical stress required to stabilize intermediate polarization states strongly depends on the accessible length scale along the stress and electric-field direction. Nevertheless, sufficiently large compressive stress can still overcome polarization fluctuations and eventually stabilize polarization states perpendicular to the electric-field direction, leading to the emergence of double hysteresis behavior.

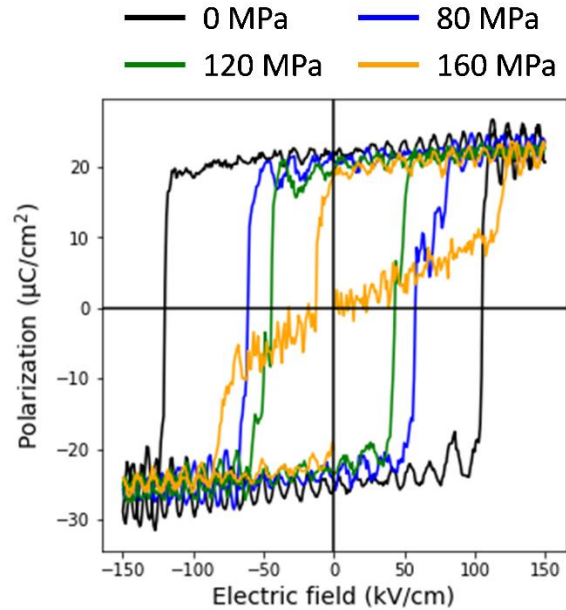


Figure 9 The P–E hysteresis loops under the *c*-axis electric field for the $8\times 8\times 32$ tetragonal BaTiO_3 supercell at 250 K under different *c*-axis compressive stresses. The black, blue, green, and orange curves correspond to compressive stresses of 0, 80, 120, and 160 MPa, respectively.

Taken together, the results presented in Sections 2.1–2.3 reveal a coherent physical picture of size-dependent polarization switching in BaTiO_3 . In small supercells, suppressed polarization fluctuations inhibit domain-wall nucleation, and switching proceeds homogeneously with relatively low coercive fields. As the supercell size increases, enhanced configurational disorder, quantified by Shannon entropy, facilitates 180° domain-wall nucleation and drives a crossover toward domain-wall-mediated switching accompanied by significantly higher coercive fields. This size-dependent transition also manifests in the electromechanical response: the critical stress required to stabilize intermediate polarization states and induce double hysteresis behavior increases with supercell dimension, while the switching pathway becomes increasingly sensitive to the relative orientation between the electric field and applied stress. These findings demonstrate that system size is not merely a computational parameter, but an intrinsic physical

variable governing polarization-switching behavior in ferroelectric BaTiO₃.

IV. CONCLUSIONS

In conclusion, this study demonstrates that polarization switching in tetragonal BaTiO₃ operates in two distinct physical regimes — homogeneous switching and domain-wall-mediated switching — and that system size is the key variable controlling which regime is operative. Using MLP-MD with the MACEField model, we showed that increasing the supercell size enhances local polarization fluctuations, quantified by Shannon entropy, which promote 180° domain-wall nucleation and raise the coercive field by over 50%. Furthermore, the switching pathway and electromechanical response are sensitive to both supercell geometry and the relative orientation of applied stress and electric field, with the critical stress for double hysteresis loop formation increasing markedly with supercell dimension. These results establish that finite-size effects are not a numerical artifact to be minimized, but a physically meaningful variable that governs domain-wall dynamics and hysteresis behavior in ferroelectric systems. From a practical standpoint, our findings suggest that atomistic simulations of ferroelectric switching must carefully consider system size to correctly capture the operative mechanism — and that the domain-wall-mediated regime, accessible only in sufficiently large supercells, may be more representative of the switching behavior observed in real ferroelectric materials and devices. Future work extending this framework to finite temperatures, defect-containing systems, and other ferroelectric compositions will further clarify the generality of the size-dependent switching transition identified here.

ACKNOWLEDGMENTS

This study was supported by the Ministry of Education, Culture, Sports, Science and Technology (MEXT) (Nos. 24H00042), and the New Energy and Industrial Technology Development Organization (NEDO). PYC would acknowledge the support of JST SPRING (Grant Number JPMJSP2108).

AUTHOR CONTRIBUTIONS

Po-Yen Chen conceptualized the work, conducted the investigation and data analysis, developed the methodology and software, visualized the results, and wrote the original draft of the manuscript. Teruyasu Mizoguchi supervised the project, acquired funding, and reviewed and edited the manuscript.

DATA AVAILABILITY

All models utilized in this work, including the MACE and MACEField models, are publicly available in our GitHub repository, Finetuned-MACE-model (<https://github.com/nmdl-mizo/Finetuned-MACE-model.git>).

APPENDIX A: Shannon entropy calculation

To quantify the degree of polarization fluctuation during the polarization-switching process, the Shannon entropy was calculated from the distribution of local Ti-displacement directions. For each MD step, the Ti-displacement vectors were first normalized into unit vectors to remove the influence of displacement magnitude and retain only the polarization orientation information. The normalized vectors were then transformed into spherical coordinates (θ, ϕ), where θ represents the polar angle and ϕ represents the azimuthal angle. The orientation distribution was discretized using a two-dimensional histogram on the spherical coordinate space with $n_{\text{bins}} \times n_{\text{bins}}$ angular grids. The probability of finding local polarization vectors within each angular region was calculated as

$$p_i = \frac{N_i}{N}$$

where N_i is the number of vectors in the i -th angular bin and N is the total number of Ti-displacement vectors. The Shannon entropy was then evaluated as

$$S = - \sum_i p_i \ln p_i$$

where the summation was performed over all nonzero probability bins. A larger Shannon entropy corresponds to a broader distribution of local polarization orientations, indicating enhanced polarization fluctuation and configurational disorder within the supercell

APPENDIX B: MaceField Model performance

The MACEfield model[27] employed in this study was developed based on our previously finetuned MACE model[26] and further trained using a BEC dataset[11] containing 2,038 solid-state BaTiO₃ structures to enable BEC prediction. The energy and atomic-force prediction accuracies of the MACEfield model are compared with those of the original MACE model in Table 1. As shown in the table, the prediction accuracies of the MACE and MACEfield models remain highly similar, with only minor improvements observed for the MACEfield model due to the additional finetuning using the solid-state dataset. These results indicate that the introduction of the BEC training does not significantly affect the energy and force prediction performance of the original MACE model. Therefore, to maintain consistency with our previous studies, the original finetuned MACE model was retained as the MLP in the present MLP-MD

*Contact author: poyen@iis.u-tokyo.ac.jp

†Contact author: teru@iis.u-tokyo.ac.jp

framework, while the MACEfield model was used specifically for BEC prediction.

Table 1 The energy and force prediction ability of the MACE model and the MACEField model.

MAE	MACE	MACEField
Energy (meV/atom)	0.85	0.43
Force (meV/Å)	17.5	14.9

In addition, we examined the phonon dispersions of the $9 \times 9 \times 9$ BaTiO₃ supercell to evaluate whether the MACEField model can reproduce long-range interaction effects, as shown in Figure 10. Four models were considered in this comparison: the original MACE model, the MACEField model finetuned from the MACE model, the MACELES model[44-48], and the MACEField model finetuned from the MACELES model. As shown in the figure, the MACEField models do not reproduce the characteristic phonon behavior near the Γ point associated with long-range electrostatic interactions, even when finetuned based on the MACELES model. These results indicate that the present MACEField framework does not explicitly capture long-range interaction effects. Nevertheless, as discussed in our previous study, long-range interactions mainly influence the quantitative properties of bulk BaTiO₃, whereas the qualitative polarization-switching behavior remains largely unchanged. Therefore, the main discussions and conclusions regarding polarization-switching mechanisms in the present study are not expected to be significantly affected by the absence of explicit long-range interactions.

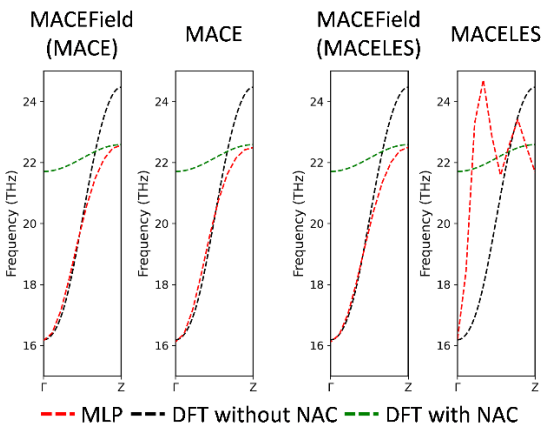


Figure 10 The phonon dispersion on the Γ -Z path calculated by the MACEField finetuned by MACE, the MACE, the MACEField finetuned by MACELES, and the MACELES model. The red, black, and green dashed lines show the results obtained by MLP, DFT without non-analytic correction (NAC), and DFT with NAC, respectively.

Next, to evaluate the performance of the MACEField model in the present workflow, we investigated its BEC prediction accuracy and compared it with the previously developed Equivar model[28,29]. The comparison results are summarized in Table 2. As shown in the table, the MACEField model exhibits improved prediction accuracy for solid-state BaTiO₃ structures compared with the Equivar model. This improvement is mainly attributed to the use of a solid-state-focused training dataset in the present MACEField model, whereas the Equivar model was additionally trained using highly distorted structures. In contrast, for highly distorted structures, the Equivar model shows better prediction performance than the MACEField model.

Table 2 The prediction ability of the Equivar model and the MACEField model for solid and highly distorted structures.

MAE (e)	Equivar model	MACEField
Solid	0.03	0.01
Highly distorted structure	0.07	0.26

To further validate the applicability of the MACEField model in electric-field MD simulations, we compared the P-E hysteresis loops obtained using the previous framework (MACE + Equivar)[11,25] and the present framework (MACE + MACEField) for the $8 \times 8 \times 8$ BaTiO₃ supercell. As shown in Figure 11, the hysteresis loops obtained using the two methods remain similar, indicating that the replacement of the Equivar model by the MACEField model does not significantly affect the polarization-switching behavior observed in our previous studies.

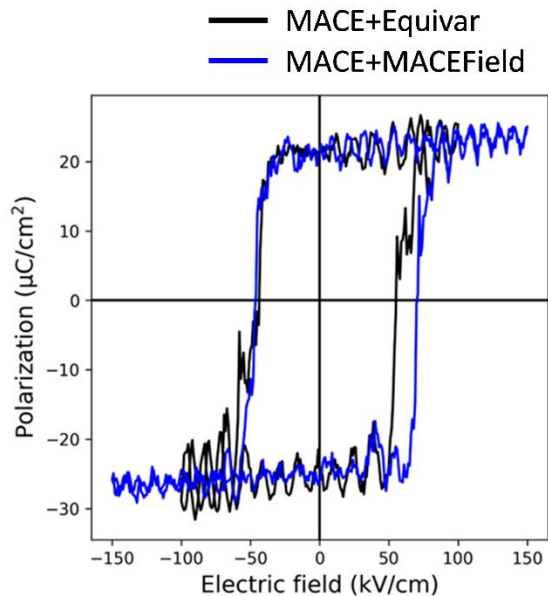


Figure 11 The hysteresis loop obtained by the MACE + Equivar model (black) and the MACE + MACEField model (blue).

The computational performance of the Equivar model and MACEField was further compared using 20k-step MD simulations for BaTiO₃ supercells with different sizes, as summarized in Figure 12. For the previous framework, the calculation time per atom per MD step gradually increases with increasing system size. In contrast, the MACEField framework maintains nearly constant computational cost as the supercell size increases, demonstrating significantly improved computational scalability for large systems. Furthermore, the application of cuEquivariance acceleration[38] provides additional improvement in computational efficiency.

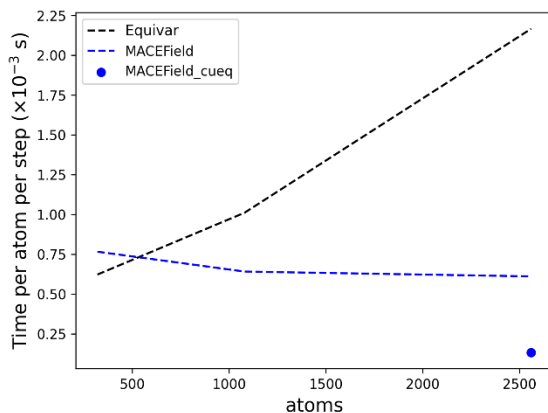


Figure 12 Number of atom-dependent calculation time. The black dashed, blue dashed, and blue point represent the Equivar model, the MACEField model, and the MACEField model with cuEquivariance acceleration.

The GPU memory usage during MD simulations is compared in Figure 13. Without acceleration, the MACEField framework requires approximately five times larger GPU memory usage than the original MACE model, reflecting the increased computational cost associated with the BEC prediction. However, after applying cuEquivariance acceleration, the GPU memory usage of the MACEField framework is significantly reduced and becomes even lower than that of the original MACE model without acceleration. These results demonstrate that the MACEField framework can provide both high prediction accuracy and high computational efficiency for electric-field MD simulations of large-scale ferroelectric systems. Therefore, the MACEField model was adopted in the present study.

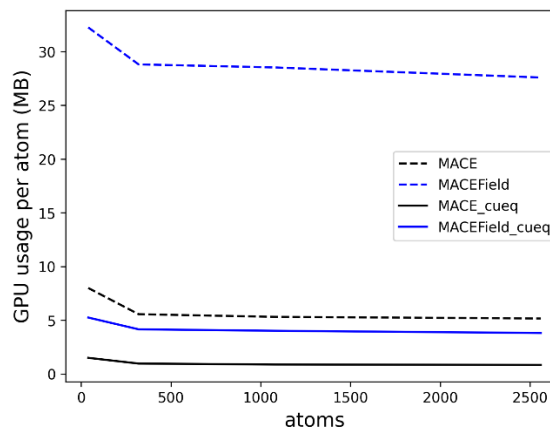


Figure 13 Number of atom-dependent GPU usage by MACE (black dashed), MACEField (blue dashed), MACE with cuEquivariance acceleration, and MACEField with cuEquivariance acceleration.

[1] A. Jain, Y. Wang, and L. Shi, JOURNAL OF ALLOYS AND COMPOUNDS **928**, 167066 (2022).

[2] M. Acosta, N. Novak, V. Rojas, S. Patel, R. Vaish, J. Koruza, G. Rossetti, and J. Rödel, APPLIED PHYSICS REVIEWS **4**, 041305 (2017).

- [3] Y. Jiang, Z. Tian, P. Kavle, H. Pan, and L. Martin, *APL MATERIALS* **12**, 041116 (2024).
- [4] M. Richman, P. Rulis, and A. Caruso, *JOURNAL OF APPLIED PHYSICS* **122**, 094101 (2017).
- [5] P. Kim, S. Han, and Y. Kang, *PHYSICAL CHEMISTRY CHEMICAL PHYSICS* **27**, 17514 (2025).
- [6] Y. Li and F. Li, *MECHANICS OF MATERIALS* **93**, 246 (2016).
- [7] W. MERZ, *PHYSICAL REVIEW* **76**, 1221 (1949).
- [8] L. Gigli, M. Veit, M. Kotiuga, G. Pizzi, N. Marzari, and M. Ceriotti, *NPJ COMPUTATIONAL MATERIALS* **8**, 209 (2022).
- [9] C. Cazorla, C. Escorihuela-Sayalero, J. Carrete, J. Iniguez-González, and R. Rurali, *ADVANCED FUNCTIONAL MATERIALS* **35** (2025).
- [10] H. Moriwake, C. A. J. Fisher, A. Kuwabara, and T. Hashimoto, *JAPANESE JOURNAL OF APPLIED PHYSICS* **50**, 09NE02 (2011).
- [11] P.-Y. Chen and T. Mizoguchi, *Materials & Design* **265**, 115851 (2026).
- [12] H. Wu, J. Zhu, and T. Zhang, *PHYSICAL CHEMISTRY CHEMICAL PHYSICS* **17**, 23897 (2015).
- [13] J. Lee, H. Song, D. Jeong, and J. Ryu, *JOURNAL OF ALLOYS AND COMPOUNDS* **1020**, 179404 (2025).
- [14] G. Deguchi, R. Kobayashi, H. Azuma, S. Ogata, M. Uranagase, and S. Spreafico, *PHYSICA STATUS SOLIDI-RAPID RESEARCH LETTERS* **18**, 2300292 (2024).
- [15] J. Shieh, J. Yeh, Y. Shu, and J. Yen, *MATERIALS SCIENCE AND ENGINEERING B-ADVANCED FUNCTIONAL SOLID-STATE MATERIALS* **161**, 50 (2009).
- [16] J. Liu, D. Yang, A. Suzana, S. Leake, and I. Robinson, *PHYSICAL REVIEW B* **111**, 054101 (2025).
- [17] B. Jiang, Y. Bai, W. Chu, Y. Su, and L. Qiao, *APPLIED PHYSICS LETTERS* **93**, 152905 (2008).
- [18] Z. Zhang, X. Qi, and X. Duan, *SCRIPTA MATERIALIA* **58**, 441 (2008).
- [19] X. Qi, H. Liu, and X. Duan, *APPLIED PHYSICS LETTERS* **89**, 092908 (2006).
- [20] D. Lourens, M. Kwaaitaal, C. Davies, and A. Kirilyuk, *REVIEW OF SCIENTIFIC INSTRUMENTS* **96**, 073701 (2025).
- [21] H. Azuma, T. Ogawa, S. Ogata, R. Kobayashi, M. Uranagase, T. Tsuzuki, and F. Wendler, *ACTA MATERIALIA* **296**, 121216 (2025).
- [22] S. Falletta, A. Cepellotti, A. Johansson, C. Tan, M. Descoteaux, A. Musaelian, C. Owen, and B. Kozinsky, *NATURE COMMUNICATIONS* **16**, 4031 (2025).
- [23] Y. Shin, I. Grinberg, I. Chen, and A. Rappe, *NATURE* **449**, 881 (2007).
- [24] Y. Li, J. Wang, and F. Li, *PHYSICAL REVIEW B* **94**, 184108 (2016).
- [25] P.-Y. Chen and T. Mizoguchi, arXiv preprint arXiv:2511.09976 (2025).
- [26] P. Chen, K. Shibata, and T. Mizoguchi, *APL MACHINE LEARNING* **3**, 036115 (2025).
- [27] B. A. Martin, A. M. Ganose, V. Kapil, T. Li, and K. T. Butler, arXiv preprint arXiv:2508.17870 (2025).
- [28] A. Kutana, K. Shimizu, S. Watanabe, and R. Asahi, *SCIENTIFIC REPORTS* **15**, 16719 (2025).
- [29] K. Shimizu, R. Otsuka, M. Hara, E. Minamitani, and S. Watanabe, *SCIENCE AND TECHNOLOGY OF ADVANCED MATERIALS: METHODS* **3**, 2253135 (2023).
- [30] I. Batatia *et al.*, *The Journal of Physical Chemistry* **163** (2025).
- [31] I. Batatia, D. Kovács, G. Simm, C. Ortner, and G. Csányi, in *ADVANCES IN NEURAL INFORMATION PROCESSING SYSTEMS 35, NEURIPS 2022* (2022).
- [32] X. Gonze and C. Lee, *PHYSICAL REVIEW B* **55**, 10355 (1997).
- [33] P. Giannozzi, S. De Gironcoli, P. Pavone, and S. Baroni, *Physical Review B* **43** (1991).
- [34] G. Kresse and J. Furthmuller, *PHYSICAL REVIEW B* **54**, 11169 (1996).
- [35] G. KRESSE and J. HAFNER, *PHYSICAL REVIEW B* **49**, 14251 (1994).
- [36] G. Kresse and J. Furthmuller, *COMPUTATIONAL MATERIALS SCIENCE* **6**, 15 (1996).
- [37] A. Larsen *et al.*, *JOURNAL OF PHYSICS-CONDENSED MATTER* **29**, 273002 (2017).
- [38] C. Ai, cuEquivariance, 2026.
- [39] S. MELCHIONNA, G. CICCOTTI, and B. HOLIAN, *MOLECULAR PHYSICS* **78**, 533 (1993).
- [40] S. Melchionna, *PHYSICAL REVIEW E* **61**, 6165 (2000).
- [41] A. Grünebohm and M. Marathe, *PHYSICAL REVIEW MATERIALS* **4**, 114417 (2020).
- [42] J. Padilla, W. Zhong, and D. Vanderbilt, *PHYSICAL REVIEW B* **53** (1996).
- [43] C. SHANNON, *BELL SYSTEM TECHNICAL JOURNAL* **27**, 379 (1948).
- [44] P.-Y. Chen and T. Mizoguchi, arXiv preprint arXiv:2603.29198 (2026).
- [45] D. Kim, X. Wang, S. Vargas, P. Zhong, D. King, T. Inizan, and B. Cheng, *JOURNAL OF CHEMICAL THEORY AND COMPUTATION* **21**, 12709 (2025).

- [46] D. King, D. Kim, P. Zhong, and B. Cheng, NATURE COMMUNICATIONS **16**, 8763 (2025).
- [47] B. Cheng, NPJ COMPUTATIONAL MATERIALS **11**, 80 (2025).
- [48] P. Zhong, D. Kim, D. King, and B. Cheng, NPJ COMPUTATIONAL MATERIALS **11**, 384 (2025).